Additive manufacturing oriented topology optimization of structures with self-supported enclosed voids

Luo, Yunfeng; Sigmund, Ole; Li, Quhao; Liu, Shutian

Published in:
Computer Methods in Applied Mechanics and Engineering

Link to article, DOI:
10.1016/j.cma.2020.113385

Publication date:
2020

Document Version
Peer reviewed version

Additive manufacturing oriented topology optimization of structures with self-supported enclosed voids

Yunfeng Luo[a], Ole Sigmund[b], Quhao Li[c], Shutian Liu[a,*]

[a]*State Key Laboratory of Structural Analysis for Industrial Equipment, Dalian University of Technology, Dalian, 116024, China*
[b]*Department of Mechanical Engineering, Solid Mechanics, Technical University of Denmark, 2800 Kgs. Lyngby, Denmark*
[c]*Key Laboratory of High-efficiency and Clean Mechanical Manufacture (Shandong University), Ministry of Education, Jinan, 250061, China*

Abstract

It is challenging to remove the supports in an enclosed void of an additively manufactured structure, while it is much easier in open regions. This paper presents a novel approach to control the minimal overhang angle only in enclosed voids in order to improve the manufacturability of AM structures with as little performance loss as possible. Firstly, a nonlinear virtual temperature method (N-VTM) is proposed to identify the enclosed voids. In the N-VTM method, void areas are assumed to be filled with a temperature-dependent heating material with high heat conductivity while the solid parts have low heat conductivity. Due to a nonlinear heat source term, the maximum temperature is controlled to a prescribed value, making the temperature in enclosed voids uniform over the whole structures. Hence, the enclosed voids can be easily identified without a careful selection of parameters. Then, the gradient of the filtered density field is applied to evaluate the overhang angle of the interface. Finally, a multiple filtering/projection process is developed to identify the overhang interface of enclosed voids, and then a logarithmic function-based constraint is developed to control overhang angle in enclosed voids by restricting the area of overhang interface of enclosed voids. Enhanced by the robust formulation, a topology optimization method for the design of structures with self-supported enclosed voids is then established. Several numerical examples are used to illustrate the effectiveness of the proposed method.

Keywords: Topology optimization, Additive manufacturing, Overhang angle, Enclosed voids.

*Corresponding author
Email address: stliu@dlut.edu.cn (Shutian Liu)

1. Introdution

Topology optimization, as an advanced design approach, has experienced rapid development in the past few decades, and several reviews can be found in [1–3]. It is capable of freely optimizing the layout of material to achieve structures with excellent performance. However, these structures obtained by topology optimization could be too complex to be manufactured. Fortunately, with the development of additive manufacturing (AM), quite complex structures can be fabricated by a layer-by-layer way. Hence, AM and topology optimization are perfectly matched.

Nevertheless, additive manufacturing still has its unique constraints which should be considered when developing a topology optimization method for additive manufacturing [4, 5]. One of the most common limitations is that supports are required to guarantee that overhang parts can be successfully manufactured for many AM processes, such as SLM (Selective Laser Melting) [6] and FDM (Fused Deposition Modeling) [7]. Naturally, post-processing is needed to remove these supports [5]. However, it is quite challenging to remove the supports in an enclosed void which often appears in optimized topologies [8, 9].

To design a simply-connected structure where the enclosed voids are removed is one of the ways to handle the problem mentioned above. To avoid the use of enclosed voids, Liu et al. [10] and Li et al. [8] proposed a so-called connectivity constraint based on a virtual thermal problem. In this method, the voids in a structure are to be filled with a virtual heating material with high heat conductivity while solid areas have low heat conductivity. Then a linear thermal problem is solved with homogeneous zero Dirichlet boundary conditions. Finally, the connectivity constraint is converted to a maximum temperature constraint. This method, labeled as virtual temperature method (VTM), has been extended to the electrode connectivity constraint [11] and the molding constraint [12]. In addition, Gaynor and Johnson [13] proposed a projection-based method to eliminate enclosed voids in topology optimization. These works are based on the density-based topology optimization. Also, the connectivity constraint was recently developed for a feature-driven topology optimization method [9] and the bi-directional evolutionary structural optimization method [14].

To design a support-free structure, which indicates all overhang angles should be larger than an allowed minimal angle, is another way that can be used to address the problem, especially for FDM, where no post-process is required to handle the enclosed voids. In the case of SLM, we still need to handle the trapped powder in the self-supported enclosed voids. However, it is still much easier to do the postprocess for the support-free enclosed voids by drilling a small hole than it is for those with supports (It is tedious and laborious

for enclosed voids and requires much bigger holes to allow the tool to go in and scrape out these supports). Much attention is being devoted to the design of support-free structures since it can not only ensure the manufacturability but also reduce the time and material costs. A simple way is through post-processing, such as the work of [15], which is effective in generating support-free structures, but at the same time the optimality of the results is compromised. Hence, the preferable way is to integrate the minimal overhang angle requirement into topology optimization processes. In density-based topology optimization, there are two main ways to handle the overhang requirement. The first strategy is to develop a support-free filter which can automatically meet the support-free requirement. For example, Gaynor and Guest [16] proposed a series of projection/filter operations based method to ensure a feature is adequately supported from below. Langelaar [17, 18] proposed a layer-wise nonlinear spatial filtering scheme to prevent the optimized structures violating self-supporting requirement. Then, Zhou et al. [19, 20] combined this AM filter and a feature-preserving filter to keep the non-designable prototype geometries unchanged. Also, Barroqueiro et al.[21] improved the AM filter in [17, 18] by using the softmax function. Ven et al.[22] developed a front propagation based filter to design support-free designs, in which unstructured meshes and the permissible degree of overhang can be freely chosen. Another strategy is to establish an overhang angle constraint to force all overhang angles to be larger than an allowed minimal angle during the optimization process. For example, Qian [23, 24] and Zhang et al. [25, 26] developed mathematical formulations of the overhang constraint by using density gradient information. Kuo and cheng [27] used a continuous logistic aggregate function to establish an overhang constraint which is based on the layer-by-layer model. Garaigordobil et al. [28, 29] developed an overhang constraint based on an edge detection algorithm, Smallest Univalue Segment Assimilating Nucleus (SUSAN). Also, the overhang-free design problem is solved in other topology optimization frameworks, such as the level set method [30–32], and some recently developed explicit methods[33, 34].

Although both the connectivity constraint and the overhang constraint are already capable of ensuring manufacturability of optimized topologies, they still have limitations. The connectivity requirement may be too strong in some cases, such as the classic stiffness problem where enclosed voids are desirable. Besides, additional supports are still required for the simply-connected structures to ensure their manufacturability and this will increase the time and material costs. As for the overhang constraint, since the supports can be relatively easily removed in open regions, we don't need to control the overhang angle in these regions from the performance perspective. Actually, the aim of this work is to take advantage of this to develop as loose an AM constraint as possible.

In this paper, a new way to constrain the overhang angle only in the enclosed voids

is proposed to compromise the manufacturability and performance. To design structures with self-supported enclosed voids, a nonlinear virtual temperature method (N-VTM) is firstly proposed to identify the enclosed voids. The maximum temperature of the nonlinear method is controlled to a prescribed value, which makes the temperature uniform in the regions covered by enclosed voids. This makes it simpler to identify all enclosed voids since we don't need to carefully select the temperature threshold. Further, the gradient information of filtered density field is used to evaluate the overhang angle. Then, a multiple filtering/projection process is proposed to identify all the interfaces that require supports. Finally, a logarithmic function-based constraint is developed to control overhang angle in enclosed voids by constraining the area of overhang interface of enclosed voids to zero. The robust formulation [35] is also applied in this paper to control the length scale of both solid and void phases and also to prevent hanging features. To save time, the nonlinear thermal analysis is implemented every 10 iterations and the sensitivity of the temperature is ignored. A detailed study motioning and supporting this simplification is also provided in an appendix. Numerical examples demonstrate the effectiveness of the proposed method.

The rest of the paper is organized as follows. In section 2, how to control overhang angle of enclosed voids is discussed, which includes the general idea, enclosed voids identification, overhang interface identification and multiple filtering/projection based constraint. In section 3, the topology optimization scheme of structures with self-supported enclosed voids is formulated and sensitivity analysis is also given. Then, several numerical examples and a conclusion are presented in Sections 4 and 5, respectively. Finally, an appendix to study the effect of sensitivities of thermal filed is also provided.

2. Controlling overhang angle of enclosed voids

2.1. General idea

In order to illustrate the general idea of how to control the minimal overhang angle of enclosed voids, we define the term "overhang interface". This defines the interface that needs added support when a structure is manufactured by additive manufacturing (AM). Mathematically, it means that the overhang angle θ of local interface is less than a specific value θ^0, as shown in Figure 1. For example, the red and blue interfaces in Figure 1 are overhang interfaces in an enclosed void and an open void, respectively. Hence, it can be naturally understood that controlling the minimal overhang angle in enclosed voids can be realized by constraining the length (2D) or area (3D) of red overhang interface in enclosed voids to zero. Now, one of the crucial issues to implement this idea is how to distinguish enclosed voids from open voids since our purpose of this work is just to control

the overhang angle in enclosed voids. Naturally, the second issue is how the overhang interfaces are identified. Section 2.2 and 2.3 illustrate how we are going to handle these two issues.

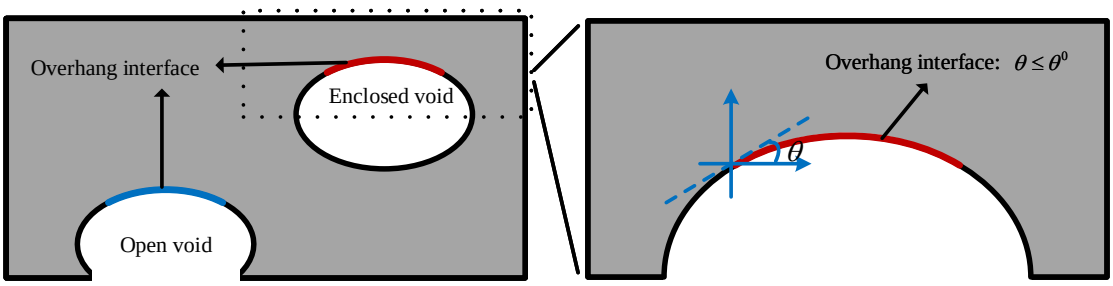

Figure 1: An example of a structure with overhang interfaces in both enclosed and open voids

2.2. Enclosed voids identification

There exists an inspiring approach, which is referred to as the virtual temperature method (VTM) [8, 10, 36], to identify enclosed voids. The idea is quite simple. That is, void areas are assumed to be filled with a high heat conductivity material with a uniformly distributed heat source, while the solid parts are treated as another type of material with low heat conductivity (near-zero). Then, enclosed voids can be distinguished from the open voids by the temperature difference. However, it is challenging to set a general temperature threshold that is capable of identifying all the enclosed voids for any design by using this linear thermal problem. This is because the temperature may vary greatly in enclosed voids due to the differences in void sizes, wall thickness, and locations.

2.2.1. Nonlinear virtual temperature method (N-VTM)

A new idea in this paper is to construct a nonlinear thermal problem to make the temperature distribution as uniform as possible in the region covered by enclosed voids. We call this method the nonlinear virtual temperature method (N-VTM). The general idea of N-VTM is shown in Figure 2 (a), which is similar to the VTM. However, in N-VTM we solve the following nonlinear problem for the temperature field T in the domain Ω

$$\begin{cases} \nabla(k\nabla T) + Q\left(T\right) = 0, & \text{in } \Omega \\ T = 0, & \text{on } \partial\Omega \end{cases} \tag{1}$$

Here, Q is a temperature-dependent heat source defined as

$$Q = \frac{q}{1 + e^{\alpha(T - T_{\max})}} \tag{2}$$

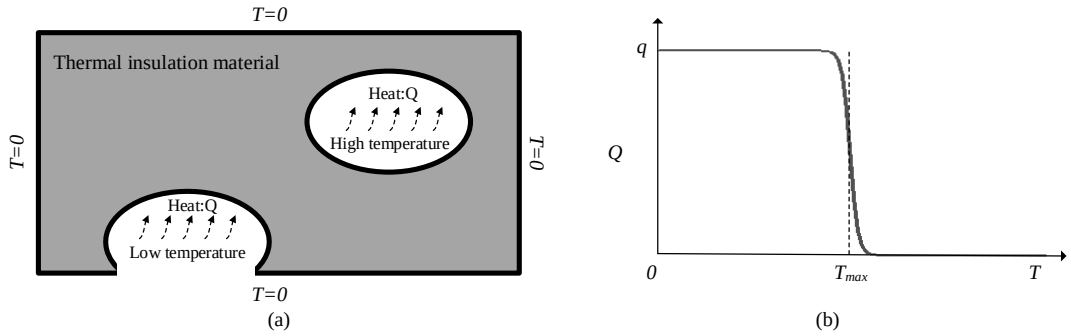

Figure 2: Nonlinear virtual temperature method (N-VTM) for enclosed void identification. (a). The general idea of N-VTM. (b). The relation between the nonlinear heat source term Q and temperature T.

where α and $T_{\max}$ are two positive numbers. A general relation between the nonlinear heat source term Q and temperature T is shown in Figure 2 (b). Besides, the parameters k and q are defined as

$$\begin{cases} k = k_0, \quad q = q_0, & \text{in void phase} \\ k = \varepsilon_0 k_0, \quad q = 0, & \text{in solid phase} \end{cases} \tag{3}$$

where k_0 and q_0 are positive reals playing the roles of conductivity and thermal source, respectively. ε_0 is an extremely small positive number to create huge difference in conduction between the void and solid phases. Finally, the following continuous interpolations are used

$$\begin{cases} k = \mu^{p_T}\varepsilon_0 k_0 + (1-\mu^{p_T})k_0 \\ q = (1-\mu^{p_T})q_0 \end{cases} \tag{4}$$

where p_T is a penalization parameter and μ is the density field.

To solve this nonlinear thermal problem, the governing equation is discretized and expressed in its residual form as

$$\mathbf{R} = \mathbf{HT} - \mathbf{Q}(\mathbf{T}) = \mathbf{0} \tag{5}$$

where $\mathbf{R}$ and $\mathbf{T}$ are the residual vector and temperature vector, respectively. $\mathbf{H}$ is the thermal conductivity matrix. The heat load $\mathbf{Q}(\mathbf{T})$ is a nonlinear temperature-dependent vector. Here, the Newton-Raphson method is applied to solve this nonlinear problem. That is, the iteration scheme can be formulated as

$$\mathbf{T}^{i+1} = \mathbf{T}^i - \frac{\mathbf{R}}{\partial \mathbf{R}/\partial \mathbf{T}} \tag{6}$$

The convergence criterion is defined as the normalized second-order norm is smaller than an allowed convergence error

$$\frac{\|\mathbf{R}\|}{\|\mathbf{R}_1\|} \leq \varepsilon_1 \tag{7}$$

where the normalization parameter $\|\mathbf{R}_1\|$ is the norm of the residual vector in the first iteration step. The error ε_1 is always set as a small value 10^{-6} in this paper.

By solving the new nonlinear thermal problem, the temperature in the region covered by enclosed voids can be controlled to the prescribed value $T_{\max}$, making the temperature uniform in the regions covered by enclosed voids. Then, the enclosed voids can be easily identified without a careful selection of temperature threshold, which is selected as a fixed value $T_{\max}/2$ in this paper. Hence, the enclosed voids can be distinguished from the open voids simply by the condition

$$T > \frac{T_{\max}}{2} \tag{8}$$

Here it should be noted that we should combine the temperature field T and the density field μ to distinguish solid phase, enclosed voids and open voids (This is not possible from only one of these two fields). This will be discussed in detail in numerical example section.

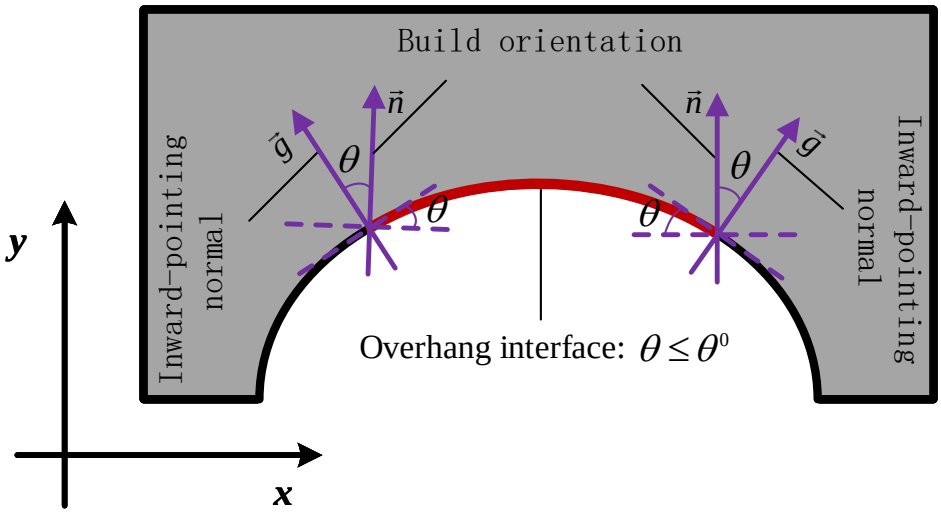

Figure 3: Overhang angle and overhang interface

2.3. Overhang Interface Identification

Identifying the local boundary angle is a popular way to design support-free structures [23, 24, 26]. In this paper, this idea is also used to identify the overhang interface. However, different from the existing approaches, a two-step process is applied to evaluate the overhang angle, where the second filtered density is used to to calculate the overhang angle. In addition, the robust approach is applied to avoid certain artifacts (i.e. hanging features and sharp corners).

As shown in Figure 3, the overhang angle θ can be generally defined as the angle between the build orientation $\vec{n} = (n_x, n_y)$ and inward-pointing normal $\vec{g}$ at an interface point.

In this paper, the inward-pointing normal is evaluated by the gradient of the filtered density field

$$\vec{g} = (\frac{\partial \tilde{\mu}}{\partial x}, \frac{\partial \tilde{\mu}}{\partial y}) \tag{9}$$

where $\tilde{\mu}$ is the filtered density. Then, the cosine of the overhang angle θ can be evaluated as

$$\cos\ \theta = \frac{\vec{n} \cdot \vec{g}}{\|\vec{n}\| \cdot \|\vec{g}\|} \tag{10}$$

The overhang interface is defined as the boundary where the overhang angle θ is less than a specific value θ^0. Also, this condition can be described as

$$\cos\ \theta - \cos\ \theta^0 > 0 \tag{11}$$

Finally, the following normalized field χ is defined to identify the overhang interface

$$\chi = 0.5 + 0.25 \cdot (\cos\theta - \cos\theta^0) \|\nabla \tilde{\mu}\|_\alpha \tag{12}$$

where the normalized norm of the gradient $\|\nabla \tilde{\mu}\|_\alpha = \alpha \|\nabla \tilde{\mu}\|$ is used to identify interface. $\|\nabla \tilde{\mu}\|_\alpha$ is in a continuous interval [0,1]. The normalization parameter α is the inverse of the maximum possible gradient norm, which is dependent on the filter radius, say $\alpha = R/\sqrt{3}$ [4]. It should also be noted that $\|\nabla \tilde{\mu}\|_\alpha$is close to 1 in the interface region at the same time it will quickly drop to 0 when going away from interface. Then, the normalized field χ is also located in [0,1]. As can be seen, the overhang interface can be identified by using

$$\chi > 0.5 \tag{13}$$

2.4. Multiple filtering/projection based constraint

In this section, a multiple filtering/projection process is firstly proposed to identify the overhang interface in enclosed voids, as shown in Figure 4. Here, the PDE filter based on a Helmholtz-type partial differential equation [37] is applied for smoothing the design variable field

$$-r^2 \nabla^2 \tilde{\rho} + \tilde{\rho} = \rho \tag{14}$$

where the length scale parameter, r, is dependent on the filter radius, R, in the standard linear filter

$$r = \frac{R}{2\sqrt{3}} \tag{15}$$

In addition, the following continuous Heaviside function [35] is used for projection

$$\overline{x} = H(x, \eta, \beta) = \frac{\tanh(\beta\eta) + \tanh(\beta(x - \eta))}{\tanh(\beta\eta) + \tanh(\beta(1 - \eta))} \tag{16}$$

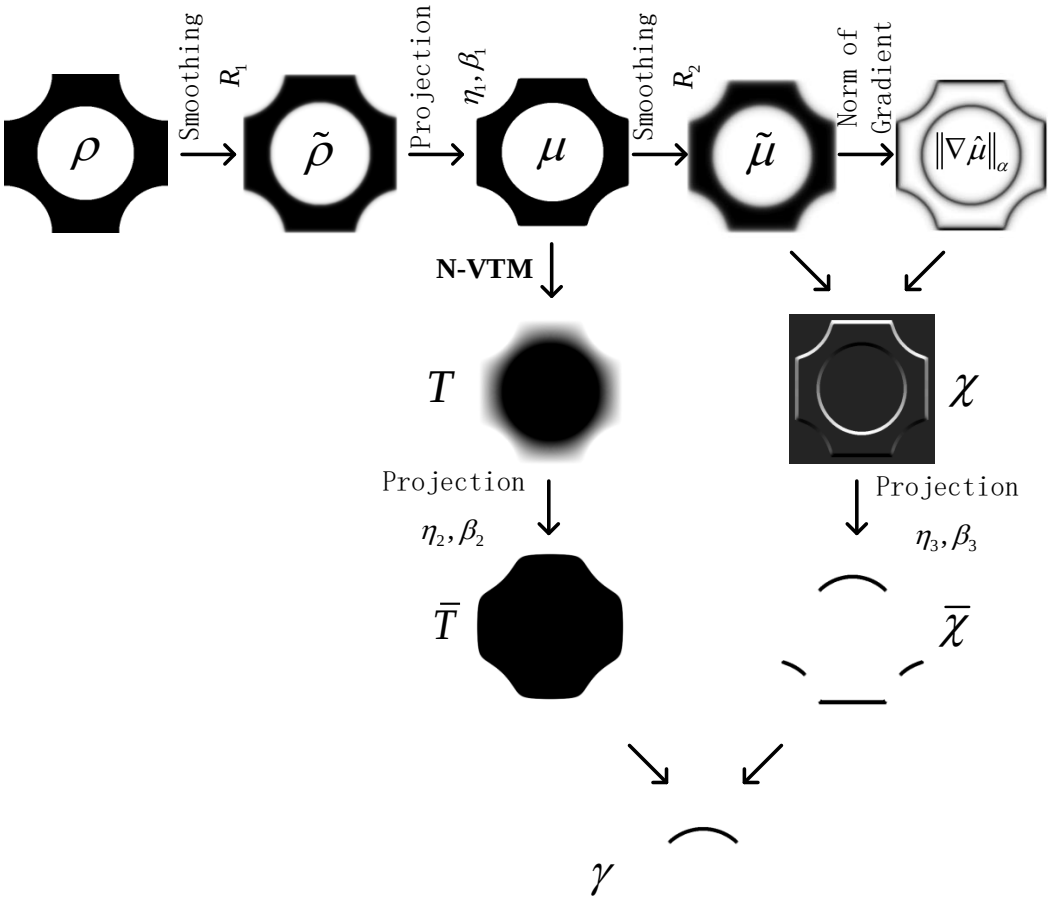

Figure 4: The multiple filtering/projection process for identifying overhang interface in enclosed voids.

where β and η determine the sharpness and threshold of the projection function.

In the proposed method, the design field, ρ, is firstly smoothed and projected, giving μ, which describes the final design. The main control parameters for these two processes are shown in Figure 4.

Next, the nonlinear virtual temperature method (N-VTM) is applied on the field μ, giving the temperature field, T. As mentioned in section 2.2, $T_{\max}/2$ is taken as the temperature threshold to identify the enclosed voids. Hence, the following projected field $\bar{T}$ is defined

$$\bar{T} = H(\frac{T}{T_{\max}}, \eta_2, \beta_2) \tag{17}$$

where β_2 is set as a fixed number 0.5 here. It can be easily understood that the enclosed voids are located in the region $\bar{T} = 1$ when the sharpness parameter η_2 goes to infinity. At the same time, the topology field, μ, is filtered again, giving $\tilde{\mu}$. Then, we can calculate the

two gradient components of $\tilde{\mu}$ by

$$\begin{pmatrix} \frac{\partial \tilde{\mu}}{\partial x} \\ \frac{\partial \tilde{\mu}}{\partial y} \end{pmatrix} = \begin{pmatrix} \frac{\partial}{\partial x} \\ \frac{\partial}{\partial y} \end{pmatrix} \mathbf{N}^T \boldsymbol{\xi} = \boldsymbol{B}\boldsymbol{\xi} \tag{18}$$

where $\boldsymbol{\xi}$ is a vector of the nodal density of the second filtered density $\tilde{\mu}$, which can be directly obtained when solving the partial differential equation of the second filter using FEM. $\mathbf{N}$ is a vector of the four shape functions.

The normalized norm of the gradient $\|\nabla\tilde{\mu}\|_\alpha$ and the cosine of the overhang angle cos θ can be obtained by using the gradient information. Then, the normalized field χ can be naturally obtained using Eq. (12). Based on Eq. 13, we use a projection with a fixed threshold 0.5 to identify the overhang interface

$$\bar{\chi} = H(\chi, \eta_3, \beta_3) \tag{19}$$

where $\eta_3 = 0.5$. Then, $\bar{\chi} = 1$ is the condition of overhang interface identification. Finally, a new field γ is defined by using $\bar{\chi}$ and $\bar{T}$

$$\gamma = \bar{T}\bar{\chi} \tag{20}$$

It can be naturally understood that the region with $\gamma = 1$ is the overhang interface in enclosed voids. Hence, we can constrain the volume of γ to zero to control the minimal overhang angle in enclosed voids, that is,

$$\sum_{e=1}^{N_e} \gamma_e = 0 \tag{21}$$

where N_e is the element numbers over the whole design domain. For easier implementation by using the MMA optimization solver, a relaxed inequality constraint is used

$$\sum_{e=1}^{N_e} \frac{\gamma_e}{N_e} \leq 10^{-r} \tag{22}$$

where r is a positive number. Besides, a logarithmic function is applied in order to enhance the convergence behavior when the constraint is close to be satisfied

$$\log_{10}(\sum_{e=1}^{N_e} \frac{\gamma_e}{N_e}) + r \leq 0 \tag{23}$$

A simple comparison between the original and logarithmic function enhanced constraints is show in Figure 5. The left-hand side of the original constraint is a function which approaches zero but is impossible to be less than or equal to zero. Satisfying such

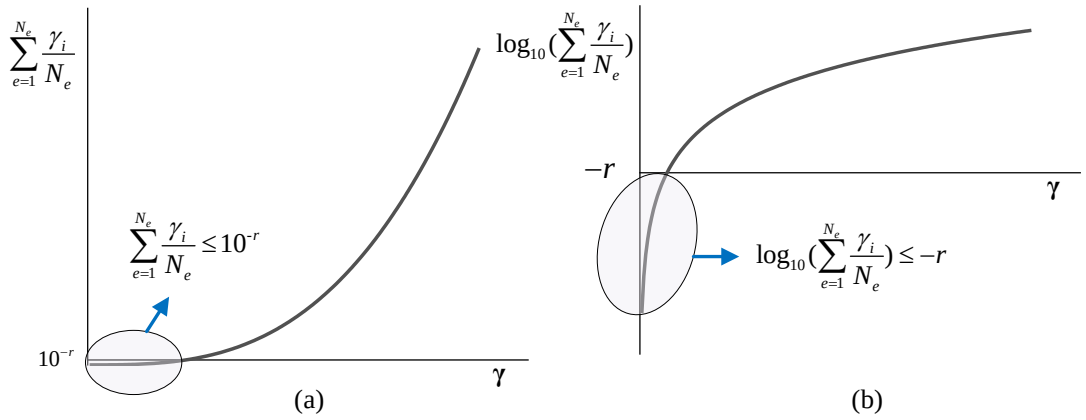

Figure 5: A comparison between the original and logarithmic function enhanced constraints.

a constraint makes the sensitivities approach zero, and thus it is hard or sometimes even impossible to satisfy it. However, from the Figure 5 (b), it can be easily understood that the logarithmic function enhanced constraint would perform better in the final stage of the optimization process.

Now, a multiple filtering/projection based constraint is established to control the minimal overhang angle in enclosed voids.

3. Robust topology optimization of structures with self-supported enclosed voids

To control the minimal length scale of both void and solid phases, we use the worst case based robust formulation [35]. Actually, controlling the minimal length scale plays an important role in this work. More specifically, it can ensure manufacturability by suppressing thin components, and at the same time, it is capable of preventing hanging features [26].

3.1. Robust optimization formulation

The robust formulation [35] is based on the eroded μ^e, intermediate μ^i and dilated μ^d designs which are given by the first projection, as shown in Figure 4, with thresholds $\eta_1^e = 0.5+\Delta\eta$, $\eta_1^i = 0.5$ and $\eta_1^d = 0.5-\Delta\eta$, respectively. More specifically, the robust formulation minimizes the worst performance of these three realizations and at the same time constrains the volume on the dilated design. By doing this, we can generate manufacturing tolerant designs with little performance loss. Also, in order to make the overhang angle constraint robust, the new overhang angle constraint is simultaneously imposed on all of the three realizations. This eliminates issues in identifying the interfaces of small or thin features

[38], and thus to add the constraint on the three realizations can improve the behavior of the constraint. Finally, the proposed method can be formulated as

$$
\begin{aligned}
&\underset{\rho}{min} : max\ (C(\boldsymbol{\mu}^e), C(\boldsymbol{\mu}^i), C(\boldsymbol{\mu}^d)) \\
&s.t.\ : \mathbf{K}^e\mathbf{U}^e{=}\mathbf{F} \\
&\quad : \mathbf{K}^i\mathbf{U}^i{=}\mathbf{F} \\
&\quad : \mathbf{K}^d\mathbf{U}^d{=}\mathbf{F} \\
&\quad : f_v(\boldsymbol{\mu}^d) = \sum_{e=1}^{N_e} \mu_e^d v_e - V_d^* \sum_{e=1}^{N_e} v_e \leq 0 \\
&\quad : f_\theta(\boldsymbol{\gamma}^e) = \log_{10}(\sum_{e=1}^{N_e} \tfrac{\gamma_e^e}{N_e}) + r \leq 0 \\
&\quad : f_\theta(\boldsymbol{\gamma}^i) = \log_{10}(\sum_{e=1}^{N_e} \tfrac{\gamma_e^i}{N_e}) + r \leq 0 \\
&\quad : f_\theta(\boldsymbol{\gamma}^d) = \log_{10}(\sum_{e=1}^{N_e} \tfrac{\gamma_e^d}{N_e}) + r \leq 0 \\
&\quad : 0 \leq \rho_i \leq 1
\end{aligned}
\tag{24}
$$

where C is the compliance. $\mathbf{K}$, $\mathbf{U}$ and $\mathbf{F}$ are global stiffness matrix, global displacement vector and global load vector, respectively. The Young's modulus of the material is modelled by the SIMP interpolation $E = \mu^p E_0 + (1 - \mu^p)E_{\min}$, where E_0 and $E_{\min}$ are the Young's moduli of solid ($\mu = 1$) and void ($\mu = 0$) phases, respectively. In order to make the volume fraction of intermediate design μ^i equal to a prescribed value V^*, the volume fraction of dilated design V_d^* is updated every 10 iterations by

$$
V_d^* = \frac{V^*}{V^i} V^d \tag{25}
$$

where V^i and V^d are the volumes of intermediate and dilated designs, respectively.

3.2. Sensitivity Analysis

First, the derivatives of the compliance with respect to the design variables, $\boldsymbol{\rho}$, can be obtained by the adjoint method as

$$
\frac{\partial C}{\partial \rho_e} = -\mathbf{U}^T \frac{\partial \mathbf{K}}{\partial \rho_e} \mathbf{U} = -\sum_i \frac{\partial E_i}{\partial \rho_e} (\mathbf{u}_i^T \mathbf{k}^0 \mathbf{u}_i) \tag{26}
$$

where $\mathbf{k}^0$ is the element stiffness matrix with unit Young's modulus, and

$$
\frac{\partial E_i}{\partial \rho_e} = q(E_0 - E_{\min}) \mu_i^{q-1} \frac{\partial \mu_i}{\partial \rho_e} \tag{27}
$$

Here, $\partial \mu_i / \partial \rho_e$ is a standard sensitivity modification factor due to the filtering and projection, which can be easily obtained by using the chain rule. Thus it is omitted here but can be found in the work of [35, 37, 38].

Another crucial part is the sensitivity of the constraint functions f_v and f_θ. The sensitivity of volume constraint f_v is very simple, which is also omitted. Next, the derivatives of f_θ with respect to the design variables, $\boldsymbol{\rho}$, can be given as

$$\frac{\partial f_\theta}{\partial \rho_e} = \frac{\sum_{i=1}^{N_e} \frac{\partial \gamma_i}{\partial \rho_e}}{\ln(10) \cdot N_e \cdot \sum_{i=1}^{N_e} \frac{\gamma_i}{N_e}} \tag{28}$$

The term $\partial \gamma_i / \partial \rho_e$ can be further developed by the product rule as

$$\frac{\partial \gamma_i}{\partial \rho_e} = \frac{\partial \bar{T}_i \bar{\chi}_i}{\partial \rho_e} = \bar{\chi}_i \frac{\partial \bar{T}_i}{\partial \rho_e} + \bar{T}_i \frac{\partial \bar{\chi}_i}{\partial \rho_e} \tag{29}$$

$\bar{T}$ is obtained by solving a nonlinear thermal problem (i). In order to save time for the nonlinear problem, $\bar{T}$ can be updated only at every N^{th} step. By doing so, the first term of (28) is equal to zero except at these discrete time steps. Hence, for simplicity, the first term can be ignored. Actually, the effect of the applied simplification is minor, and a detailed study on this is provided in appendix A. Now, $\partial \gamma_i / \partial \rho_e$ can be rewritten as

$$\frac{\partial \gamma_i}{\partial \rho_e} = \bar{T}_i \frac{\partial \bar{\chi}_i}{\partial \rho_e} \tag{30}$$

Then, $\partial \bar{\chi}_i / \partial \rho_e$ can be obtained by the chain rule as

$$\frac{\partial \bar{\chi}_i}{\partial \rho_e} = 0.25\alpha \frac{\partial \bar{\chi}_i}{\partial \chi_i} [(\frac{n_x}{\|\vec{n}\|} - \frac{\cos\theta^0}{\|\vec{g}\|} \frac{\partial \tilde{\mu}_i}{\partial x}) \frac{\partial}{\partial \rho_e} (\frac{\partial \tilde{\mu}_i}{\partial x}) + (\frac{n_y}{\|\vec{n}\|} - \frac{\cos\theta^0}{\|\vec{g}\|} \frac{\partial \tilde{\mu}_i}{\partial y}) \frac{\partial}{\partial \rho_e} (\frac{\partial \tilde{\mu}_i}{\partial y})] \tag{31}$$

where

$$\frac{\partial}{\partial \rho_e} (\frac{\partial \tilde{\mu}_i}{\partial x}) = \frac{\partial}{\partial \rho_e} (\mathbf{B}^x \boldsymbol{\xi}_i) = \sum_{k=1}^{n} B_k^x \frac{\partial \xi_{ik}}{\partial \rho_e} \tag{32}$$

$$\frac{\partial}{\partial \rho_e} (\frac{\partial \tilde{\mu}_i}{\partial y}) = \frac{\partial}{\partial \rho_e} (\mathbf{B}^y \boldsymbol{\xi}_i) = \sum_{k=1}^{n} B_k^y \frac{\partial \xi_{ik}}{\partial \rho_e} \tag{33}$$

Here, $\mathbf{B}^x$ and $\mathbf{B}^y$ are two rows of $\mathbf{B}$, as shown in Eq. (17). n is the node number corresponding to element i. $\partial \xi_{ik} / \partial \rho_e$ also represents a standard modification factor of sensitivities for filtering and projection. Now all required terms for the sensitivity analysis are given above. Note that no adjoint solution is required as the sensitivity of temperature is ignored. The adjoint solution based sensitivity without ignoring the sensitivity with respect to the temperature field can be found in appendix A.

4. Numerical examples

In this section, several numerical examples are provided to show the effectiveness of the proposed method. For simplicity, the uniform mesh with element size 1×1 is applied for the design domains of all the following examples. Besides, the material properties of elastic mechanical problem are also fixed as $E = 1$, $\mu = 0.3$. Regarding the parameters for the nonlinear virtual thermal problem, $k_0 = 1$ and $\varepsilon_0 = 10^{-9}$ are used to model thermal conductivity of void and solid phases. The heat source parameter $T_{\max}$ is arbitrarily given, and then we scale q_0 such that the maximum temperature of the linear thermal analysis on the void domain is equal to $\alpha T_{\max}$. Here $T_{\max} = 100$ and $\alpha = 0.2$ are applied for all examples. In addition, the two filter radii for smoothing, R_1 and R_2, are both fixed as 10. The sharpness parameter of the first projection, β_1, is updated by a factor 1.3 at every 10th step (or at convergence) from 1 to 128, while the other two sharpness parameters, β_2 and β_3, are handled equivalently where the only difference is the initial values which are 16.

The structure can be divided into three parts based on the projected temperature field $\bar{\mathrm{T}}$ and density field μ, i.e. solid phase is identified by by μ= 1, enclosed void by μ= 0 and $\bar{\mathrm{T}} = 1$ (or $(1-\mu)\bar{\mathrm{T}} = 1$), open void by μ= 0 and $\bar{\mathrm{T}} = 0$ (or $(1-\mu)(1-\bar{\mathrm{T}}) = 1$). In addition, the solid phase (μ=1) can also be divided into two parts, i.e. overhang interface by μ=1 and $\bar{\chi} = 1$ (or $\mu\bar{\chi} = 1$) and the remaining part by μ=1 and $\bar{\chi} = 0$(or $\mu(1-\bar{\chi}) = 1$). Hence, we use the following field τ to plot our results

$$\tau = 1\mu\bar{\chi} + \frac{2}{3}\mu(1-\bar{\chi}) + \frac{1}{3}(1-\mu)\bar{\mathrm{T}} + 0\,(1-\mu)(1-\bar{\mathrm{T}}) \tag{34}$$

In this way, different colors can be used to represent different parts, as discussed further below.

4.1. MBB

The first example is the MBB design problem. The dimensions of the design domain can be found in Figure 6. Solid passive domains are applied at all supports and loads. Homogeneous zero Dirichlet boundary conditions have been prescribed for both the PDE filter and the nonlinear thermal analysis.

The optimization problem is solved with a volume fraction of 50%, a build orientation $\vec{n} = (0, 1)$, a threshold of overhang angle $\theta^0 = \pi/4$ and a constraint relaxation parameter r=2.

Figure 7 shows the optimized structures with three different robust parameters ($\Delta\eta = 0$, 0.1 and 0.2). As can be seen, there exist several thin features and hanging features that

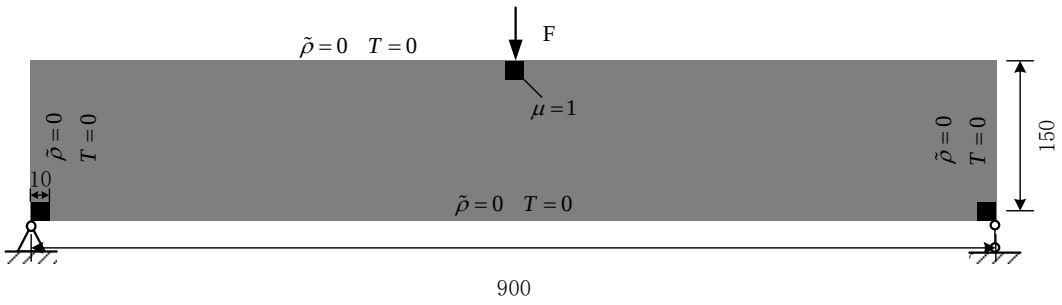

Figure 6: the design domain of the MBB example

are not manufacturable in the result with $\Delta\eta = 0$, i.e. without using robust scheme. Due to the robust scheme, these features disappear with little decrease in performance (the compliances for the three designs are 198.07, 203.65 and 212.71, respectively).

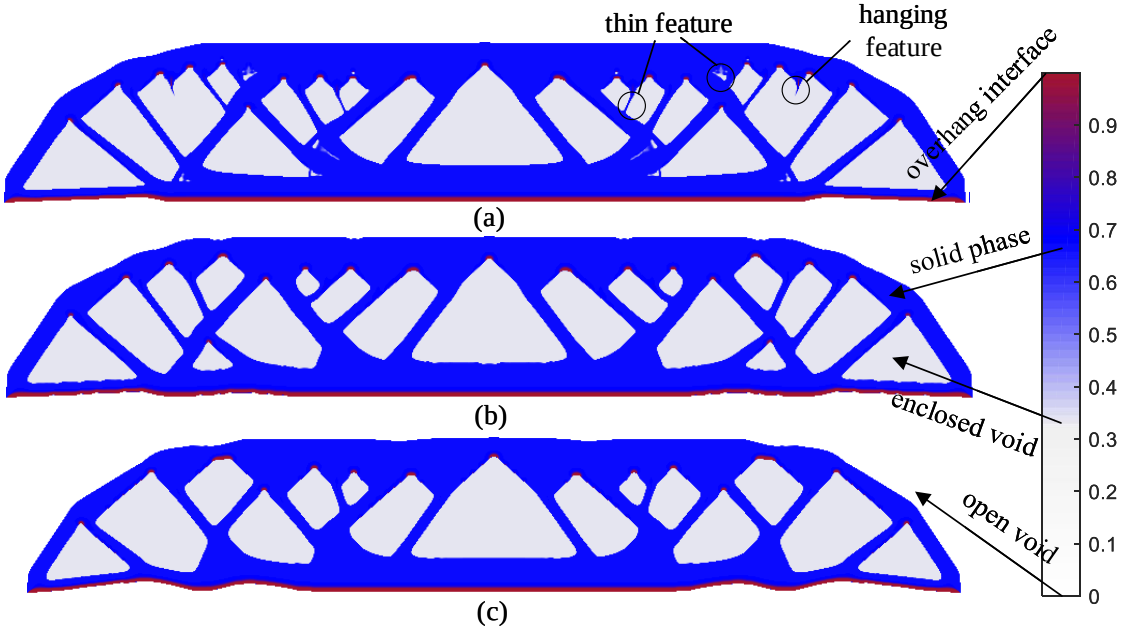

Figure 7: The optimized results with varying robust parameters. (a). $\Delta\eta = 0$, $C = 198.07$(without robust formulation). (b). $\Delta\eta = 0.1$, $C = 203.65$. (c). $\Delta\eta = 0.2$, $C = 212.71$. The applied color bar illustrates the mapping from the value of the field τ to the color. The red, blue, gray and white respectively represents overhang interface, solid phase, enclosed void and open voids, and this is same for all the following examples.

The color bar in Figure 7 illustrates the mapping from the value of the field τ to the color. As can be seen, the red, blue, gray and white represents overhang interface, solid phase, enclosed void and open voids, respectively, and this is same for all the following examples. From the results, we can see that the overhang angle is bigger than the allowed

minimal angle in enclosed voids except the upper corners that actually have no manufacturability issues. Since the overhang angle isn't constrained in open voids in the proposed method, there is a very long interface that needs supports but can be easily removed.

The case, where zero Neumann boundaries are applied for the PDE filter at all outer edges while other optimization parameters are set as the same with that of Figure 7 (b), is also solved here. As shown in Figure 8, the bottom edges are straight for this case which is different from Figure 7 (b). Interestingly, the compliance of this design is even a little bigger than the design with wavy edges. Actually, this has been carefully studied in the work of Clausen and Andreassen [39]. We have all been lured into believe that bottom edges are always straight and follow design domain boundary. But that is due to filtering BC's that make structure attract to boundary. If we do it right and add a passive domain outside the design domain as suggested in [39], we will get optimal structures that are "wavy". Hence, we believe that the waviness is a witness of correct topologies.

Figure 8: The optimized result with zero Neumann boundaries for the PDE filter, while other optimization parameters are the same as those of Figure 7 (b). The final compliance is $C = 206.08$.

To illustrate the importance of the proposed nonlinear virtual temperature method, an optimized result using the linear method is also given here, as shown in Figure 9. As can be seen, the linear method failed to constrain the minimal overhang angle for the two enclosed holes close to the supports. In order to show the difference between the linear and nonlinear method, the temperature distributions of both results with linear and nonlinear method are given in Figure 10. As seen, the maximum temperature of the nonlinear thermal problem is controlled to the prescribed value $T_{\max} = 100$, which makes the temperature quite uniform in the region covered by enclosed voids. However, the temperature obtained by the linear method varies greatly in the enclosed void region. Hence, it can be easily understood that, compared to the linear method, the nonlinear method has an advantage in distinguishing the enclosed voids from the open voids since it is easier to determine a right temperature threshold and a normalization factor. The reason for the failing of the result in Figure 9 is that the temperature in the two critical voids is smaller than the prescribed threshold.

The iteration histories of the compliance and constraints are also given in Figure 11 to show the convergence behavior of the proposed method. It can be seen that the compliance

Figure 9: The optimized structure with linear virtual temperature method.

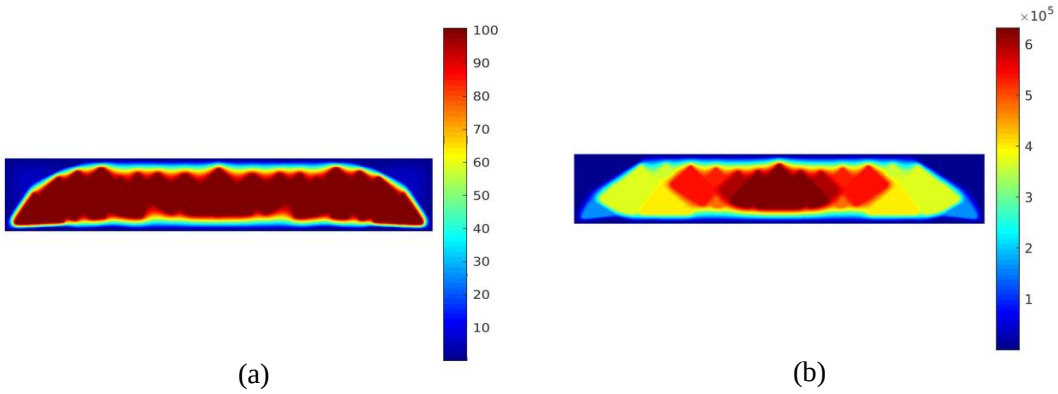

Figure 10: (a). The temperature distribution of the nonlinear method corresponding to the design (b) in Figure 6. (b). The temperature distribution of the linear method corresponding to the design in Figure 7.

and constraints are smoothly converged at iteration 182. Here it should be noted that the overhang constraint isn't active in the very beginning of the optimization process as there are very many gray elements and no voids. In addition, the history of the computational cost of the nonlinear thermal analysis is also given in Figure 11. On one hand, although the thermal problem is a nonlinear problem, the computational cost is acceptable compared to the linear elastic FE since there is only one degree of freedom corresponding to each node in the thermal problem. As an example, the CPU time of the linear elastic FE for the design (b) in Figure 7 is 1.16 seconds while the nonlinear thermal analysis takes 0.97 seconds for total 5 nonlinear iterations. It should be noted that, compared to the linear elastic FE, the CPU time of the nonlinear problem will be relatively smaller when going to 3D. Also, the nonlinear analysis is performed only every 10th step in the current method, thus, the computational cost is essentially ignorable.

4.2. Cantilever beam

As shown in Figure 12, this benchmark example is a cantilever beam design problem. A solid passive domain is applied at the load. The default boundary conditions can be found in Figure 10. That is, homogeneous Dirichlet boundary conditions are applied for nonlinear thermal analysis. Regarding the PDE filter, a zero Neumann boundary is used for the wall

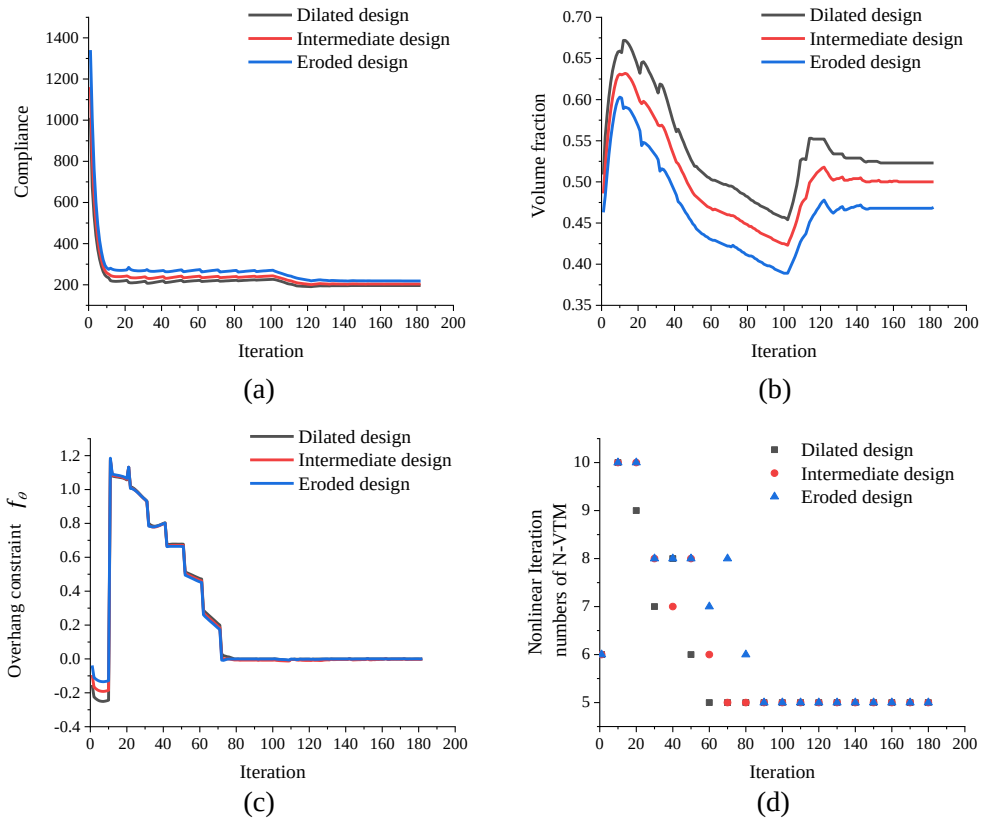

Figure 11: Iteration histories of compliance, constraints and computational cost of N-VTM

while zero Dirichlet boundary conditions are applied on the remaining boundaries. All the details can be found in Figure 12. A volume fraction of 50% is used in this example.

Figure 11 shows the optimized results with a same build orientation $\vec{n} = (0, 1)$ but different allowed minimal overhang angles, i.e. $\theta^0 = \pi/4$ and $\pi/3$. It can be seen that the minimal overhang angle constraint only works in the enclosed voids for both cases, which demonstrates the effectiveness of the proposed method. Also, it can be naturally understood that the compliance becomes bigger with the increase of the allowed minimal angle. The practical angle threshold is dependent on the applied material and process, which should be decided from experiments.

Besides, the optimization problem is also solved with a fixed allowed minimal overhang angle $\theta^0 = \pi/4$, but different build orientations, i.e. $\vec{n} = (1, 1)$ and $(0, -1)$. The optimized structures and corresponding temperature are shown in Figure 12. As can be seen, the build orientation has a great influence on optimized topologies, especially the shapes of the enclosed voids. Also, it should be noted that the build orientation has a great influence on the amount of support material. Hence, the build orientation is a very important factor such that it should be simultaneously optimized, but this is beyond our interest in this

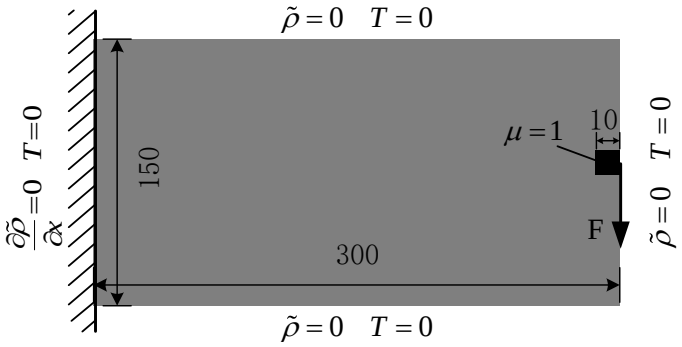

Figure 12: The design domain of the cantilever beam

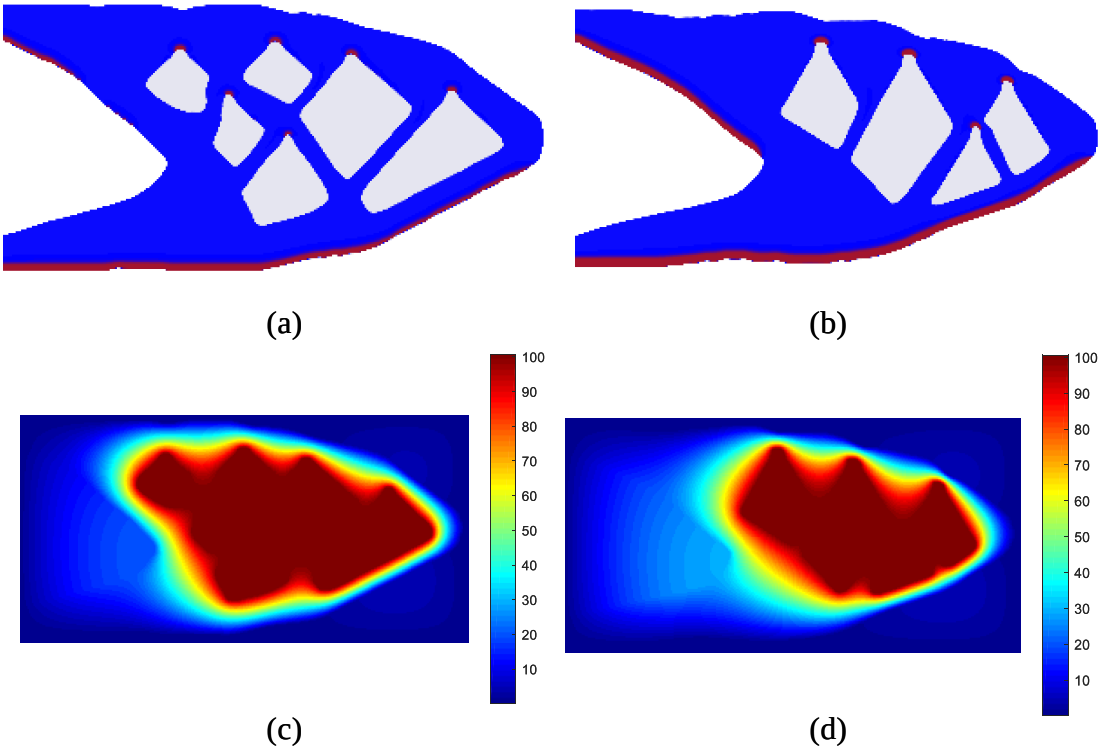

Figure 13: (a) and (b) show optimized structures with different allowed minimal overhang angles, while (c) and (d) are the temperature fields of designs (a) and (b), respectively. (a). $\theta^0 = \pi/4$, $C = 67.64$. (b). $\theta^0 = \pi/3$, $C = 73.55$.

study.

Next, we will discuss the influence of boundary conditions on the optimized results. In the above results, the homogeneous zero Dirichlet boundary conditions are applied for the PDE filter to force a gradient at outer boundaries. Thus, the interface close to the baseplate can be handled as the overhang interface where supports are required. Now, zero Neumann boundaries are prescribed for all outer boundaries. In this way, the interface close

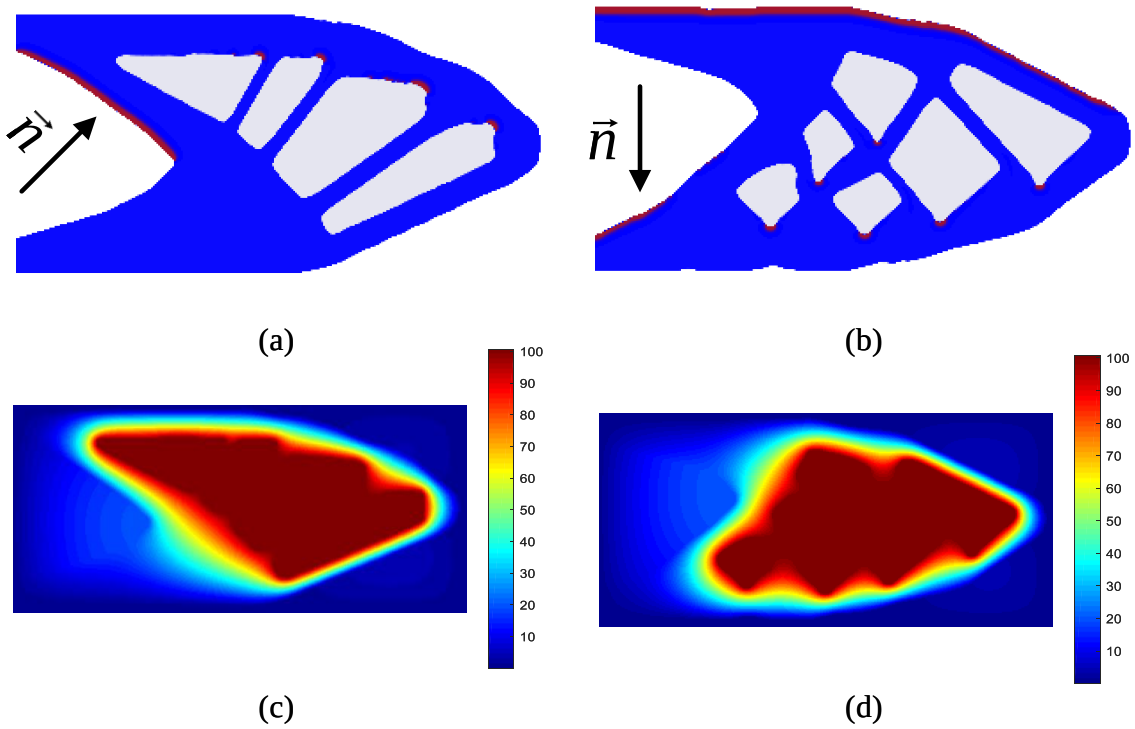

Figure 14: (a) and (b) show the optimized structures with different build orientations, while (c) and (d) are the temperature fields of designs (a) and (b), respectively. (a). $\vec{n} = (1, 1)$, $C = 65.66$. (b). $\vec{n} = (0, -1)$, $C = 67.64$.

to the baseplate is considered to be self-supported (actually supported by the baseplate). In addition, three different boundary conditions for the nonlinear analysis are considered. The boundary conditions and corresponding results are shown in Figure 15. As seen, the result (a1) is obtained by setting all boundaries as zero Dirichlet boundaries. In this result, there are two outer interfaces that require supports. But when the left boundary is isolated, the left big void is handled as enclosed void and thus is self-supported, as shown in Figure 15 (b1). The last case is that all outer boundaries are prescribed as isolated boundaries. Besides, in order to avoid singularity, the load point is set as a zero Dirichlet point ($T = 0$). As seen, all voids are handled as enclosed voids for this case, and thus the result (c1) is self-supported over the whole structure. For better understanding of the results, the corresponding temperature fields are also given in Figure 15.

4.3. T-shaped beam

This example is a T-shaped beam design problem, as shown in Figure 16. For simplicity, a rectangle design domain with two passive void domains is applied to handle the optimization problem. Homogeneous Dirichlet boundary conditions are prescribed at the boundaries of the real T-shaped domain for the nonlinear thermal analysis, while the homo-

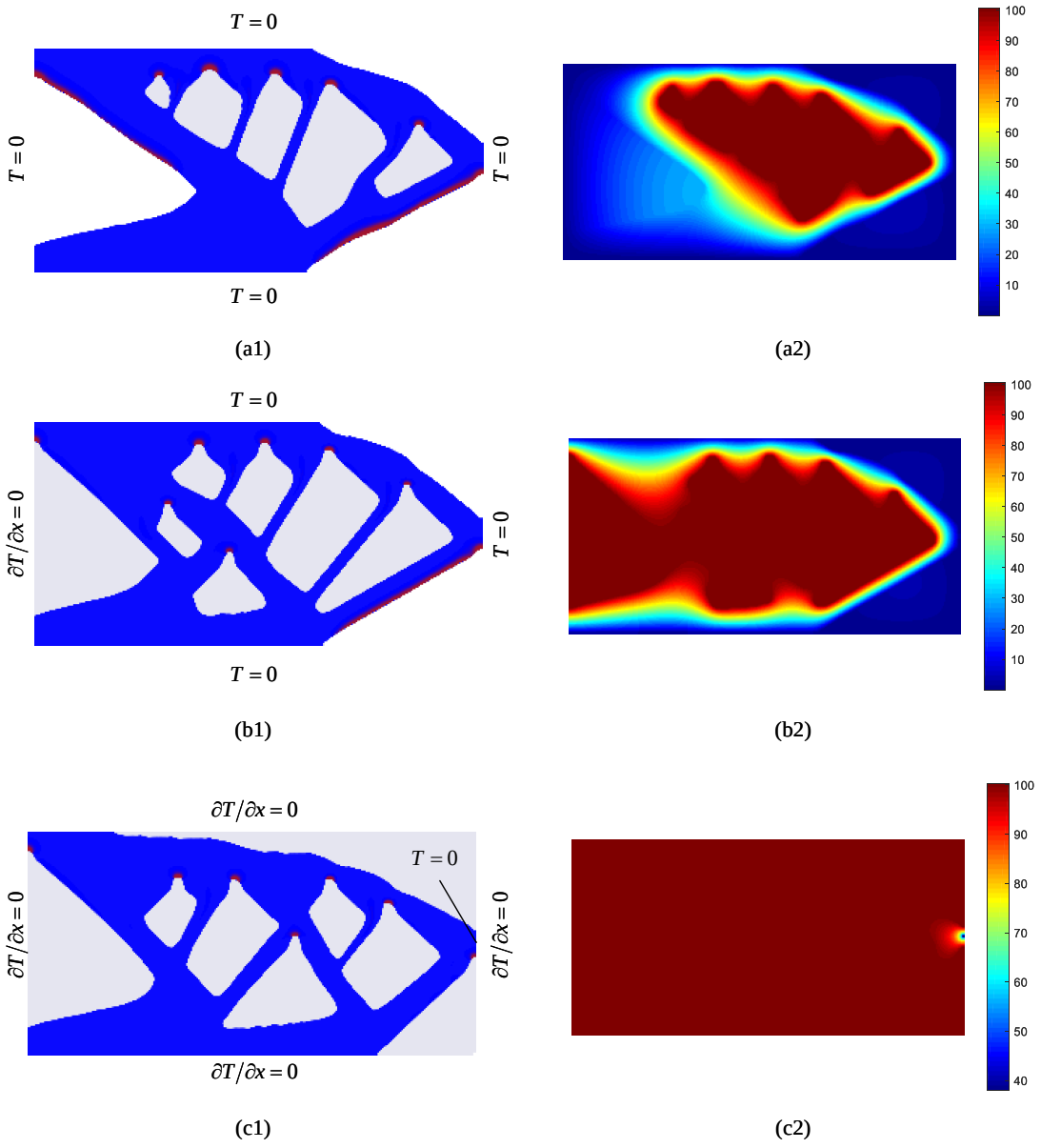

Figure 15: Optimized results with different boundary conditions. (a1), (b1) and (c1) are the optimized topologies, while (a2), (b2) and (c2) are their corresponding temperature distributions. (a1). $C = 68.08$ (b1). $C = 69.04$. (c1). $C = 70.76$.

geneous Dirichlet boundary conditions are applied at the boundaries of the whole rectangle domain for the PDE filter. More details, like the support and load information, can be found in Figure 16.

The optimization is solved with a volume fraction of 50%, a build orientation $\vec{n} = (0, 1)$, a threshold of overhang angle $\theta^0 = \pi/4$, a constraint relaxation parameter $r = 2$ and a robust parameter $\Delta\eta = 0.1$.

The optimized result and its corresponding temperature field are shown in Figure 17.

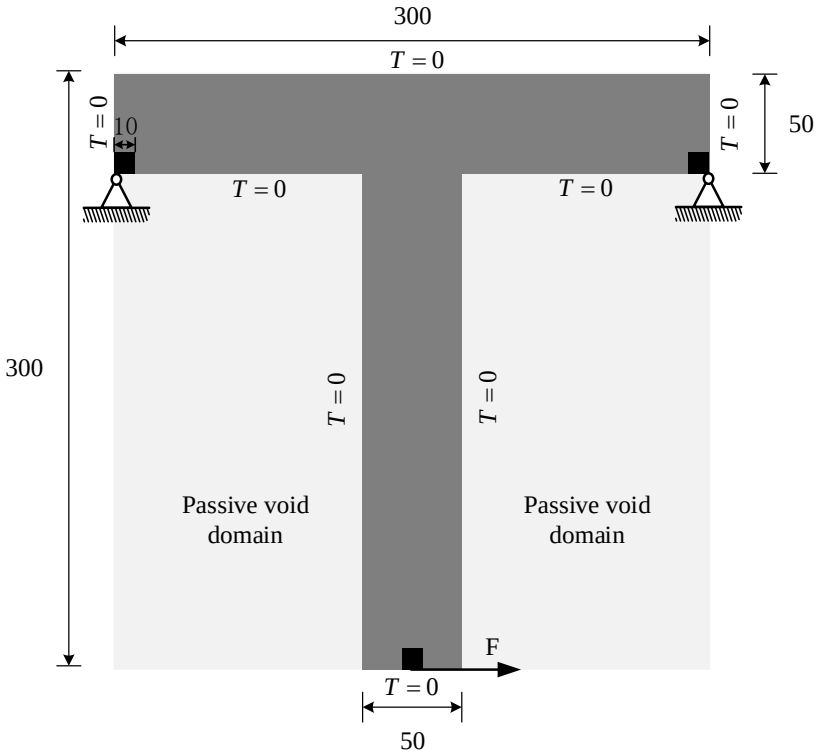

Figure 16: The design domain of the T-shaped beam.

As seen, the temperature is also uniform in the region covered by enclosed voids for this example, making it easier to control the minimal overhang angle in the enclosed voids. Also, additional supports are still needed in the upper interfaces of the applied two passive void domains, but they can be easily removed. Here it should be noted that this example is a special case where it is impossible to be self-supporting over the whole structure due to the two passive void domains. Now, to constrain the overhang angle only in enclosed voids is an alternative to handle this type of problems.

5. Conclusion

This paper provides a novel method for topology optimization of structures with self-supported enclosed voids. The general idea is to constrain the length of overhang interface in enclosed voids to zero. In order to realize this idea, a nonlinear virtual temperature method is firstly proposed to distinguish the enclosed voids from open voids. Compared to the existing linear method, the proposed nonlinear approach performs much better since the temperature is uniform (close to the prescribed $T_{\max}$) in the region covered by enclosed voids. Besides, the gradients of filtered density field are used to evaluate the overhang angle. Then, a multiple filtering/projection process is developed to identify the overhang interface in the enclosed voids. Finally, a new constraint based on a logarithmic function is

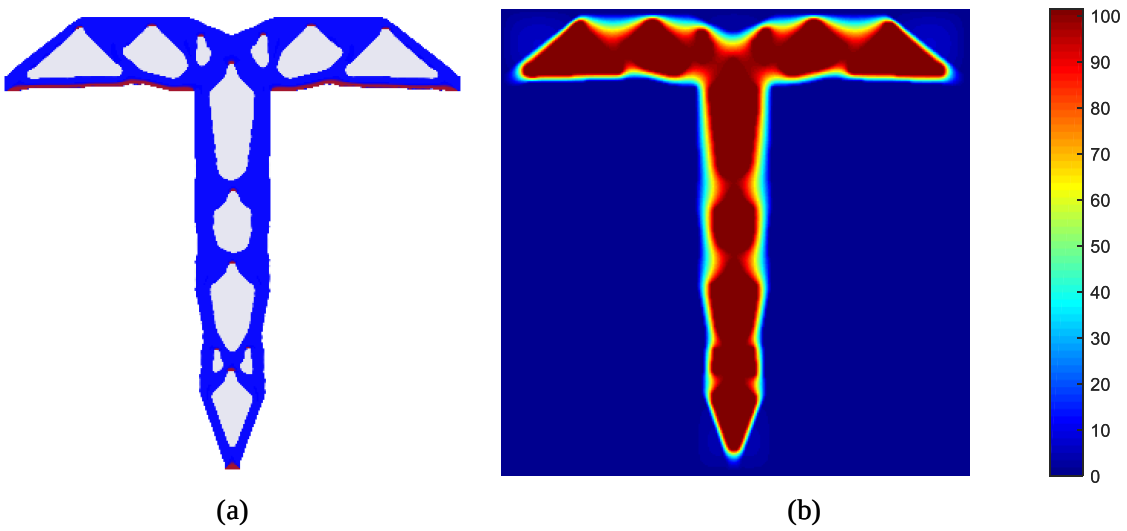

Figure 17: The optimized structure (a) and the corresponding temperature field (b).

developed to control the minimal overhang angle in enclosed voids by restricting the length of overhang interface of enclosed voids. The robust topology optimization scheme is also applied to control the minimal length scale of both solid and void phases, an at the same time is capable of preventing hanging features over the whole structure. The temperature field is updated only every 10 steps and corresponding sensitivity is also ignored to save time in this paper. A detailed study in the appendix shows the impact of the simplification being minor. The effectiveness of the proposed approach has been illustrated by several benchmark examples.

The build orientation has a great influence on the optimized topologies and the amount of the required supports in open voids. It would also be interesting to develop a method to make the enclosed voids self-supported, and at the same time use as few supports as possible in open voids, by simultaneously designing the topologies and build orientations.

The proposed nonlinear virtual temperature method (N-VTM) is expected to be applicable to a broader range of problems where the enclosed and open voids should be treated differently, such as the load dependent problem where the pressure is only loaded on outer or inner interfaces.

Acknowledgments

Yunfeng Luo acknowledges the financial support from China Scholarship Council. Ole Sigmund acknowledges the support from the Villum Foundation through the Villum Investigator Project InnoTop. This work is also supported by the National Natural Science Foundation of China (Grant Nos.U1808215,11802164).

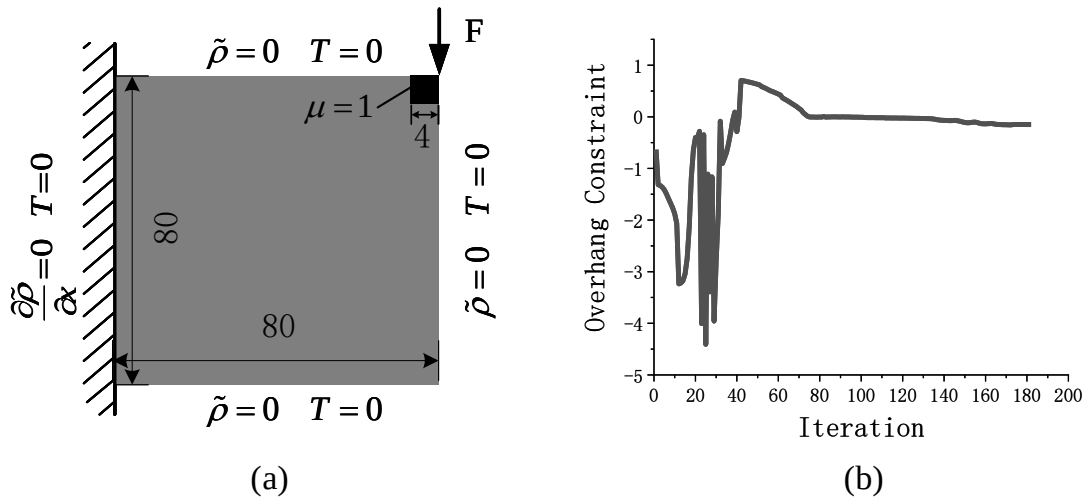

Figure A1: (a). The design domain. (b). The iteration history of overhang constraint without ignoring the sensitivity of temperature.

Appendix A: Study on the effect of sensitivities with respect to thermal field

A1. Sensitivity analysis

In this section, we study the effect of the sensitivity of the temperature field, and demonstrate why we can update T at only every 10th step and ignore its sensitivity to save time.

To derive the analytical sensitivity of the overhang constraint function f_θ, an equivalent function is established here by using the Lagrange multiplier $\mathbf{\Lambda}$ and the nonlinear thermal equilibrium equation

$$L{=}f_\theta + \mathbf{\Lambda}^T(\mathbf{HT}-\mathbf{Q}) \tag{A1}$$

The derivative of L with respect to the variable μ_e can be given as

$$\begin{aligned}\frac{\partial L}{\partial \mu_e} &= \frac{\partial f_\theta}{\partial \bar{\mathbf{T}}}\frac{\partial \bar{\mathbf{T}}}{\partial \mathbf{T}}\frac{\partial \mathbf{T}}{\partial \mu_e} + \frac{\partial f_\theta}{\partial \bar{\boldsymbol{\chi}}}\frac{\partial \bar{\boldsymbol{\chi}}}{\partial \mu_e} + \mathbf{\Lambda}^T(\frac{\partial \mathbf{H}}{\partial \mu_e}\mathbf{T} + \mathbf{H}\frac{\partial \mathbf{T}}{\partial \mu_e} - \frac{\partial \mathbf{Q}}{\partial \mu_e} - \frac{\partial \mathbf{Q}}{\partial \mathbf{T}}\frac{\partial \mathbf{T}}{\partial \mu_e}) \\ &= (\frac{\partial f_\theta}{\partial \bar{\mathbf{T}}}\frac{\partial \bar{\mathbf{T}}}{\partial \mathbf{T}} + \mathbf{\Lambda}^T\mathbf{H} - \mathbf{\Lambda}^T\frac{\partial \mathbf{Q}}{\partial \mathbf{T}})\frac{\partial \mathbf{T}}{\partial \mu_e} + \frac{\partial f_\theta}{\partial \bar{\boldsymbol{\chi}}}\frac{\partial \bar{\boldsymbol{\chi}}}{\partial \mu_e} + \mathbf{\Lambda}^T(\frac{\partial \mathbf{H}}{\partial \mu_e}\mathbf{T} - \frac{\partial \mathbf{Q}}{\partial \mu_e})\end{aligned} \tag{A2}$$

where $\mathbf{\Lambda}$ is selected as a solution of the following adjoint state equation

$$(\mathbf{H} - \frac{\partial \mathbf{Q}}{\partial \mathbf{T}})\mathbf{\Lambda} = -(\frac{\partial f_\theta}{\partial \bar{\mathbf{T}}}\frac{\partial \bar{\mathbf{T}}}{\partial \mathbf{T}})^T \tag{A3}$$

Then, the derivative of L can be rewritten as

$$\frac{\partial L}{\partial \mu_e}{=}\frac{\partial f_\theta}{\partial \bar{\boldsymbol{\chi}}}\frac{\partial \bar{\boldsymbol{\chi}}}{\partial \mu_e} + \mathbf{\Lambda}^T(\frac{\partial \mathbf{H}}{\partial \mu_e}\mathbf{T} - \frac{\partial \mathbf{Q}}{\partial \mu_e}) \tag{A4}$$

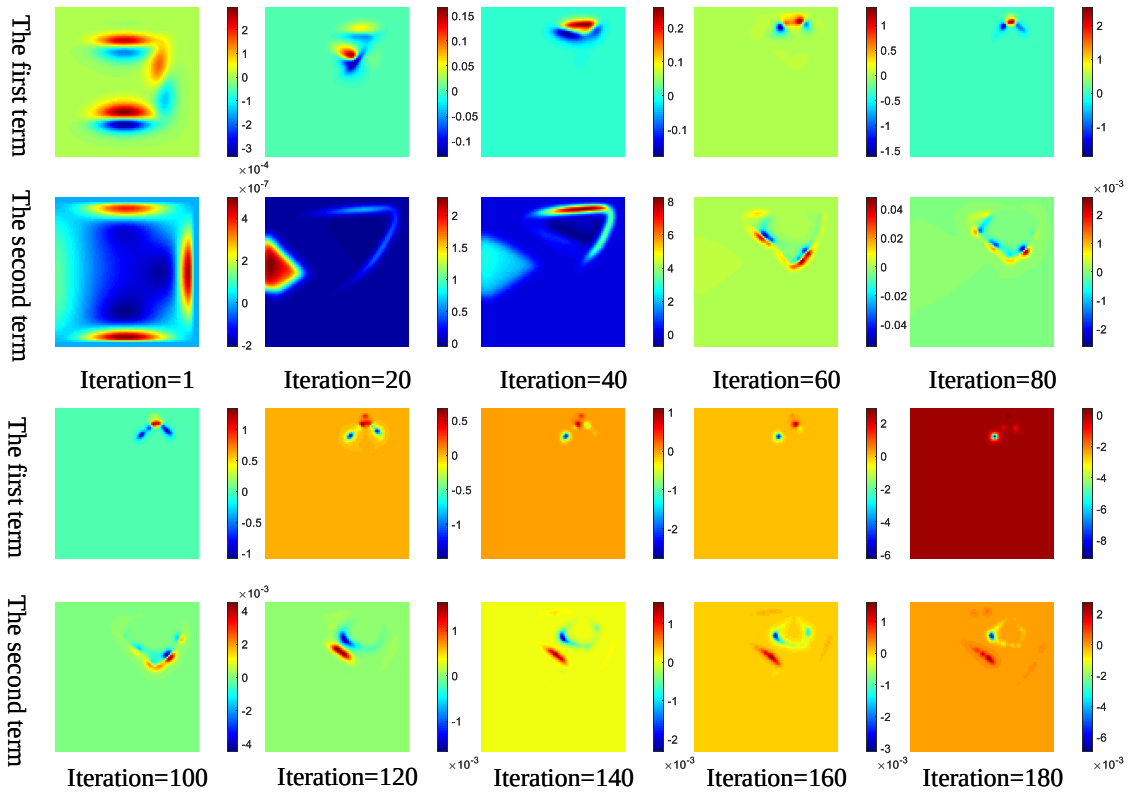

Figure A2: The first and second terms of (A. 5) during the optimization process. They are on the same order of magnitude in the very beginning (iteration<60). When iteration>60, the magnitude of the second term is much smaller than that of the first term.

Finally, the analytical sensitivity of the overhang constraint function with respect to the design variable ρ_e can be obtained by using the chain rule

$$\frac{\partial f_\theta}{\partial \rho_e} = \frac{\partial f_\theta}{\partial \bar{\boldsymbol{\chi}}} \frac{\partial \bar{\boldsymbol{\chi}}}{\partial \boldsymbol{\mu}} \frac{\partial \boldsymbol{\mu}}{\partial \tilde{\boldsymbol{\rho}}} \frac{\partial \tilde{\boldsymbol{\rho}}}{\partial \rho_e} + \boldsymbol{\Lambda}^T \left(\frac{\partial \mathbf{H}}{\partial \boldsymbol{\mu}} \mathbf{T} - \frac{\partial \mathbf{Q}}{\partial \boldsymbol{\mu}} \right) \frac{\partial \boldsymbol{\mu}}{\partial \tilde{\boldsymbol{\rho}}} \frac{\partial \tilde{\boldsymbol{\rho}}}{\partial \rho_e} \tag{A5}$$

where the first term is actually the sensitivity used in section 3.2, while the second term is the sensitivity induced by the nonlinear thermal problem.

A2. A numerical example

A design problem is used here to illustrate why we can ignore the sensitivity of temperature field in the optimization process. As shown in Fig. A1 (a), a square design domain with the load applied at the upper right corner is applied in this example. Firstly, we run the optimization with update of thermal field every iteration by using the sensitivities obtained by Eq. A5. The distributions of the first and second terms of Eq. A5 during the optimization process are given in Fig. A2. As seen, although they are on the same order of magnitude in the very beginning ($iteration < 40$), the overhang constraint is inactive in the early stage (as can be seen from Fig. A1 (b)). This is because there are so many

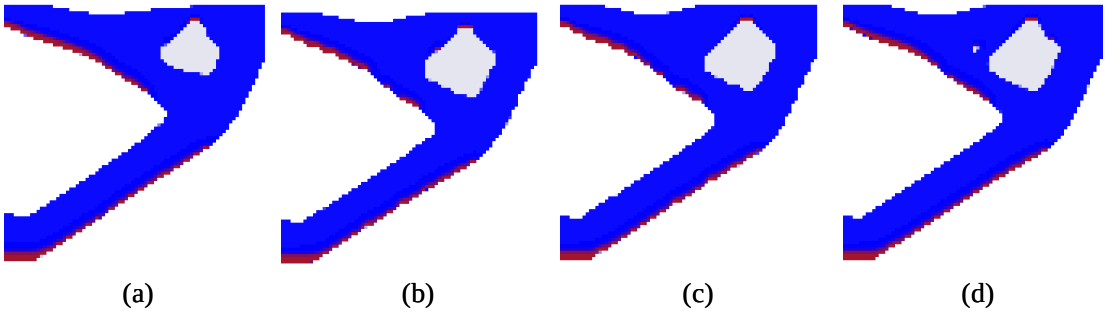

Figure A3: The optimized structures for different optimization strategies. (a) Run with update of thermal field every iteration and consider consistent sensitivities with respect to the thermal field, $C = 26.93$. (b) Run with update of thermal field every iteration but ignore the sensitivities of the thermal field, $C = 27.18$. (c) Run with update of thermal field every 10 iterations and ignore the sensitivities of the thermal field $C = 27.08$. (d) Take design (c) as a starting guess and then run with update of thermal field every iteration and consider consistent sensitivities of the thermal field, $C = 26.89$.

gray elements and the enclosed voids can't be identified in the very beginning. That is to say, the topology is mainly driven by the objective and mass constraint in the beginning of the optimization process. When $iteration > 60$, the sensitivity value of the second term is three orders of magnitude lower than that of the first term. Say, the sensitivities of the thermal field can be ignored when the overhang constraint becomes active. Hence, it can be naturally understood that the sensitivities of the thermal filed can be ignored during the whole optimization process.

Actually, this can also be seen from Eq. (29). The temperature field related term of Eq. (29) can be rewritten as

$$\bar{\chi}_i \frac{\partial \bar{T}_i}{\partial \rho_e} = \bar{\chi}_i \frac{\partial \bar{T}_i}{\partial T_i} \frac{\partial T_i}{\partial \rho_e} \tag{A6}$$

For a black-white design, $\bar{\chi}_i$ equals to one in the region of overhang interface, while it is zero in the remaining domains. At the same time, T_i is close to zero in the open interface region, while it is close to $T_{\max}$ in the enclosed interface region. That is to say, $\partial \bar{T}_i / \partial T_i$ is close to zero in interfaces when the Heaviside function of the projection is relatively sharp as the temperature in these interfaces is close to the upper and lower bounds. Hence, it can be easily seen from these facts that Eq. (A6) will be close to zero when the structure gets more discrete. Hence, this can to a certain degree support the above findings.

In order to further illustrate this, four numerical experiments are given here, as shown in Fig. A3. More specifically, design (a) is obtained by updating temperature field every iteration and considering sensitivities with respect to the thermal field. Design (b) is obtained by updating temperature field also every iteration but ignoring the sensitivities of the thermal field. Design (c) is obtained by the approach suggested in this paper, i.e.

updating thermal field every 10 iterations and ignoring the sensitivities of the thermal field. Design (d) is obtained by taking design (c) as a starting guess and then running the optimization of case (a). As seen, the compliances of the four designs are extremely close, and thus this can again support the conclusion that the sensitivities of the thermal field can be ignored. Hence, the influence of the simplification by updating thermal field every 10 iterations is minor, but this can save optimization time.

References

[1] G. I. N. Rozvany, A critical review of established methods of structural topology optimization, Structural and Multidisciplinary Optimization 37 (2009) 217–237. doi:10.1007/s00158-007-0217-0.

[2] O. Sigmund, K. Maute, Topology optimization approaches, Structural and Multidisciplinary Optimization 48 (2013) 1031–1055. doi:10.1007/s00158-013-0978-6.

[3] N. P. Van Dijk, K. Maute, M. Langelaar, F. Van Keulen, Level-set methods for structural topology optimization: a review, Structural and Multidisciplinary Optimization 48 (2013) 437–472. doi:10.1007/s00158-013-0912-y.

[4] J. Liu, A. T. Gaynor, S. Chen, Z. Kang, K. Suresh, A. Takezawa, L. Li, J. Kato, J. Tang, C. C. L. Wang, L. Cheng, X. Liang, A. C. To, Current and future trends in topology optimization for additive manufacturing, Structural and Multidisciplinary Optimization (2018). doi:10.1007/s00158-018-1994-3.

[5] M. K. Thompson, G. Moroni, T. Vaneker, G. Fadel, R. I. Campbell, I. Gibson, A. Bernard, J. Schulz, P. Graf, B. Ahuja, F. Martina, Design for additive manufacturing: Trends, opportunities, considerations, and constraints, CIRP Annals 65 (2016) 737–760. doi:10.1016/j.cirp.2016.05.004.

[6] J.-P. Kruth, P. Mercelis, J. V. Vaerenbergh, L. Froyen, M. Rombouts, Binding mechanisms in selective laser sintering and selective laser melting, Rapid prototyping journal 11 (2005) 26–36.

[7] I. Zein, D. W. Hutmacher, K. C. Tan, S. H. Teoh, Fused deposition modeling of novel scaffold architectures for tissue engineering applications, Biomaterials 23 (2002) 1169–1185.

[8] Q. Li, W. Chen, S. Liu, L. Tong, Structural topology optimization considering connectivity constraint, Structural and Multidisciplinary Optimization (2016). doi:10.1007/s00158-016-1459-5.

[9] L. Zhou, W. Zhang, Topology optimization method with elimination of enclosed voids, Structural and Multidisciplinary Optimization 60 (2019) 117–136. doi:10.1007/s00158-019-02204-y.

[10] S. Liu, Q. Li, W. Chen, L. Tong, G. Cheng, An identification method for enclosed voids restriction in manufacturability design for additive manufacturing structures, Frontiers of Mechanical Engineering 10 (2015) 126–137. doi:10.1007/s11465-015-0340-3.

[11] A. Donoso, J. K. Guest, Topology optimization of piezo modal transducers considering electrode connectivity constraints, Computer Methods in Applied Mechanics and Engineering 356 (2019) 101–115. doi:https://doi.org/10.1016/j.cma.2019.07.012.

[12] Q. Li, W. Chen, S. Liu, H. Fan, Topology optimization design of cast parts based on virtual temperature method, Computer-Aided Design 94 (2018) 28–40. doi:https://doi.org/10.1016/j.cad.2017.08.002.

[13] A. T. Gaynor, T. E. Johnson, Eliminating occluded voids in additive manufacturing design via a projection-based topology optimization scheme, Additive Manufacturing 33 (2020) 101149. doi:https://doi.org/10.1016/j.addma.2020.101149.

[14] Y. Xiong, S. Yao, Z.-L. Zhao, Y. M. Xie, A new approach to eliminating enclosed voids in topology optimization for additive manufacturing, Additive Manufacturing 32 (2020) 101006. doi:https://doi.org/10.1016/j.addma.2019.101006.

[15] M. Leary, L. Merli, F. Torti, M. Mazur, M. Brandt, Optimal topology for additive manufacture: A method for enabling additive manufacture of support-free optimal structures, Materials & Design 63 (2014) 678–690. doi:10.1016/j.matdes.2014.06.015.

[16] A. T. Gaynor, J. K. Guest, Topology optimization considering overhang constraints: Eliminating sacrificial support material in additive manufacturing through design, Structural and Multidisciplinary Optimization 54 (2016) 1157–1172. doi:10.1007/s00158-016-1551-x.

[17] M. Langelaar, Topology optimization of 3d self-supporting structures for additive manufacturing, Additive Manufacturing 12 (2016) 60–70. URL: https://dx.doi.org/10.1016/j.addma.2016.06.010. doi:10.1016/j.addma.2016.06.010.

[18] M. Langelaar, An additive manufacturing filter for topology optimization of print-ready designs, Structural and Multidisciplinary Optimization 55 (2017) 871–883. doi:10.1007/s00158-016-1522-2.

[19] M. Zhou, Y. Liu, Z. Lin, Topology optimization of thermal conductive support structures for laser additive manufacturing, Computer Methods in Applied Mechanics and Engineering 353 (2019) 24–43. doi:10.1016/j.cma.2019.03.054.

[20] M. Zhou, Y. Liu, C. Wei, Topology optimization of easy-removal support structures for additive manufacturing, Structural and Multidisciplinary Optimization (2020). doi:10.1007/s00158-020-02607-2.

[21] B. Barroqueiro, A. Andrade-Campos, R. Valente, Designing self supported slm structures via topology optimization, Journal of Manufacturing and Materials Processing 3 (2019) 68.

[22] E. van de Ven, R. Maas, C. Ayas, M. Langelaar, F. van Keulen, Continuous front propagation-based overhang control for topology optimization with additive manufacturing, Structural and Multidisciplinary Optimization (2018). doi:10.1007/s00158-017-1880-4.

[23] X. Qian, Undercut and overhang angle control in topology optimization: A density gradient based integral approach, International Journal for Numerical Methods in Engineering 111 (2017) 247–272. doi:10.1002/nme.5461.

[24] C. Wang, X. Qian, W. D. Gerstler, J. Shubrooks, Boundary slope control in topology optimization for additive manufacturing: For self-support and surface roughness, Journal of Manufacturing Science and Engineering 141 (2019) 091001. doi:10.1115/1.4043978.

[25] K. Zhang, G. Cheng, Three-dimensional high resolution topology optimization considering additive manufacturing constraints, Additive Manufacturing 35 (2020) 101224. doi:https://doi.org/10.1016/j.addma.2020.101224.

[26] K. Zhang, G. Cheng, L. Xu, Topology optimization considering overhang constraint in additive manufacturing, Computers & Structures 212 (2019) 86–100. doi:10.1016/j.compstruc.2018.10.011.

[27] Y.-H. Kuo, C.-C. Cheng, Self-supporting structure design for additive manufacturing by using a logistic aggregate function, Structural and Multidisciplinary Optimization (2019). doi:10.1007/s00158-019-02261-3.

[28] A. Garaigordobil, R. Ansola, J. Santamaría, I. F. de Bustos, A new overhang constraint for topology optimization of self-supporting structures in additive manufacturing, Structural and Multidisciplinary Optimization 58 (2018) 2003–2017.

[29] A. Garaigordobil, R. Ansola, E. Veguería, I. Fernandez, Overhang constraint for topology optimization of self-supported compliant mechanisms considering additive manufacturing, Computer-Aided Design 109 (2019) 33–48.

[30] G. Allaire, C. Dapogny, R. Estevez, A. Faure, G. Michailidis, Structural optimization under overhang constraints imposed by additive manufacturing technologies, Journal of Computational Physics 351 (2017) 295–328. doi:https://doi.org/10.1016/j.jcp.2017.09.041.

[31] J. Liu, A. C. To, Deposition path planning-integrated structural topology optimization for 3d additive manufacturing subject to self-support constraint, Computer-Aided Design 91 (2017) 27–45.

[32] Y. Wang, J. Gao, Z. Kang, Level set-based topology optimization with overhang constraint: Towards support-free additive manufacturing, Computer Methods in Applied Mechanics and Engineering (2018). doi:10.1016/j.cma.2018.04.040.

[33] X. Guo, J. Zhou, W. Zhang, Z. Du, C. Liu, Y. Liu, Self-supporting structure design in additive manufacturing through explicit topology optimization, Computer Methods in Applied Mechanics and Engineering 323 (2017) 27–63.

[34] W. Zhang, L. Zhou, Topology optimization of self-supporting structures with polygon features for additive manufacturing, Computer Methods in Applied Mechanics and Engineering 334 (2018) 56–78. doi:https://doi.org/10.1016/j.cma.2018.01.037.

[35] F. Wang, B. S. Lazarov, O. Sigmund, On projection methods, convergence and robust formulations in topology optimization, Structural and Multidisciplinary Optimization 43 (2010) 767–784. doi:10.1007/s00158-010-0602-y.

[36] A. Donoso, J. K. Guest, Topology optimization of piezo modal transducers considering electrode connectivity constraints, Computer Methods in Applied Mechanics and Engineering 356 (2019) 101–115. URL: https://dx.doi.org/10.1016/j.cma.2019.07.012. doi:10.1016/j.cma.2019.07.012.

[37] B. S. Lazarov, O. Sigmund, Filters in topology optimization based on helmholtz-type differential equations, International Journal for Numerical Methods in Engineering 86 (2011) 765–781. doi:10.1002/nme.3072.

[38] Y. Luo, Q. Li, S. Liu, Topology optimization of shell–infill structures using an erosion-based interface identification method, Computer Methods in Applied Mechanics and Engineering 355 (2019) 94–112. doi:https://doi.org/10.1016/j.cma.2019.05.017.

[39] A. Clausen, E. Andreassen, On filter boundary conditions in topology optimization, Structural and Multidisciplinary Optimization 56 (2017) 1147–1155. doi:10.1007/s00158-017-1709-1.